energies

MDPI

Article

Salt Dissolution–Induced Permeability Enhancement and Its Implications for Improved Oil Recovery During Waterflooding in Saline Lacustrine Carbonate Reservoirs

Hua Wu [1], Chenguang Cao [1,*], Bo Yin [1], Liang Zhang [1], Lishi Huang [1], Manting Zhang [1], Boyu Wang [1] and Xiao Wang [2]

[1] The Institute of Exploration and Development of SINOPEC Jianghan Oilfield Company, Wuhan 430223, China
[2] Hubei Provincial Key Laboratory of Oil and Gas Exploration and Development Theory and Technology, China University of Geosciences, Wuhan 430074, China
* Correspondence: caochg.jhyt@sinopec.com

Abstract

Waterflooding in saline lacustrine carbonate reservoirs frequently induces dissolution of soluble salt minerals, a process that substantially alters pore architecture and transport properties. However, the quantitative relationship between salt dissolution, permeability evolution, and ultimate oil recovery remains incompletely characterized. In this study, high-temperature, high-pressure core-flooding experiments were combined with numerical simulation to investigate the salt dissolution–induced permeability enhancement (SDPE) effect. Core samples from the Qianjiang Formation, containing 8–15% soluble salts, were tested under reservoir conditions (temperatures up to 100 °C, confining pressure up to 25 MPa). The results show that dissolution of halite and anhydrite cements preferentially enlarges pore throats in the 0.01–1 μm range, as confirmed by NMR T_2 spectra. Based on these observations, a time-dependent permeability model was developed using cumulative water throughput per grid as the key leading to a permeability increase of up to 170%, and was implemented as a user-defined module in the commercial reservoir simulator Comparative simulations between the conventional constant-permeability model and the time-dependent model reveal that accounting for the SDPE effect increases predicted cumulative water injection by 25%, expands sweep volume by 18 percentage points, and improves ultimate oil recovery by 4.5 percentage points over 15 years of production. These findings demonstrate that the SDPE effect is a practically exploitable mechanism for improving waterflood performance in salt-bearing carbonate reservoirs, and provide a quantitative framework for optimizing waterflooding design.

Keywords: saline lacustrine carbonate; salt dissolution; time-dependent permeability; cumulative water throughput; waterflooding; enhanced oil recovery

Check for updates

Academic Editor: Nikolaos Koukouzas

Received: 25 August 2026
Revised: 2 October 2026
Accepted: 8 October 2026
Published: 14 October 2026

Copyright: © 2026 by the authors. Licensee MDPI, Basel, Switzerland. This article is an open access article distributed under the terms and conditions of the Creative Commons Attribution (CC BY) license.

1. Introduction

Carbonate reservoirs hosted in saline lacustrine basins constitute a substantial proportion of hydrocarbon resources in continental sedimentary systems, particularly in the Cenozoic petroliferous basins of Central and East Asia [1–3]. The Jianghan Basin in central China is a representative example, where the Qianjiang Formation hosts significant oil accumulations in lacustrine carbonate intervals with cumulative thicknesses of 128–173 m [1]. Unlike their marine counterparts, saline lacustrine carbonates commonly exhibit complex

mineral assemblages in which dolomite, calcite, and authigenic clays are intimately intergrown with evaporitic minerals such as halite, anhydrite, gypsum, and glauberite [4–6]. These soluble constituents occupy intergranular pores, line micro-fractures, and coat grain boundaries, thereby exerting an outsized influence on petrophysical properties that is disproportionate to their volumetric abundance [2,6]. The Qianjiang Formation, in particular, displays total soluble salt contents ranging from 8% to 15% by weight, with halite and anhydrite as the dominant soluble phases [7–10].

Waterflooding remains the most widely deployed secondary recovery strategy in such reservoirs, largely owing to its operational simplicity, low capital intensity, and established field infrastructure [11]. In conventional sandstone and non-saline carbonate systems, the displacement process is reasonably well described by fractional-flow theory and relative-permeability relationships under immiscible conditions [12]. However, in salt-bearing carbonate formations, the injected water is almost invariably undersaturated with respect to the resident evaporitic minerals. This thermodynamic disequilibrium drives progressive dissolution of the soluble mineral fraction via $NaCl\ (s) \rightleftharpoons Na^+ + Cl^-$ and $CaSO_4\ (s) \rightleftharpoons Ca^{2+} + SO_4{}^{2-}$, with dissolution proceeding while the aqueous phase remains undersaturated relative to the mineral solubility product, a process that continuously modifies the porous medium during displacement [13,14]. We refer to this phenomenon as the salt dissolution–induced permeability enhancement (SDPE) effect. The consequent evolution of pore architecture can manifest as either enhanced injectivity and improved sweep or as the development of preferential flow conduits that exacerbate channeling and early water breakthrough [15,16].

Previous experimental and numerical investigations have addressed several isolated aspects of this phenomenon; their key findings, methods and limitations are summarized in the text to clarify the remaining knowledge gap. On the mineralogical side, batch-reactor and core-flooding studies have established that the dissolution kinetics of halite are several orders of magnitude faster than those of anhydrite and gypsum, and that dissolution rates are governed principally by the degree of undersaturation, temperature, and specific surface area [17,18]. Pore-network modeling studies have suggested that dissolution preferentially enlarges the largest, most connected pore throats, yielding a power-law increase in permeability as a function of dissolved porosity [19,20]. On the recovery side, several field-scale simulation studies have reported that reactive transport during waterflooding can either increase or decrease ultimate recovery depending on the spatial distribution of soluble minerals and the injection strategy [21,22].

Despite this progress, two important gaps persist. First, there is a scarcity of systematically controlled experiments that simultaneously track permeability evolution, pore-structure change, and oil recovery within a single integrated framework under reservoir-representative temperature and pressure conditions. The majority of existing core-flooding studies have been conducted at ambient or moderate temperatures, and the behavior of salt dissolution under high-temperature (up to 100 °C) and high-pressure (up to 25 MPa) conditions—which are characteristic of the deeper intervals of the Qianjiang Formation—remains largely unexplored. Second, competing hypotheses remain unresolved regarding the net impact of salt dissolution on macroscopic recovery. One hypothesis emphasizes the beneficial permeability enhancement, arguing that dissolution opens previously inaccessible pore space and improves lateral and vertical connectivity [23,24]. An alternative hypothesis contends that the creation of high-conductivity dissolution channels is inherently detrimental, as it reduces the pressure gradient available to displace oil from the rock matrix and accelerates water breakthrough at the producing well [25,26].

A third gap, which is perhaps most significant from a practical standpoint, concerns the representation of the SDPE effect in reservoir simulation. Conventional numerical

simulators treat permeability as a static property that does not evolve during the flooding process. Under this assumption, waterflooding in low-permeability carbonate reservoirs is typically predicted to become increasingly difficult over time, with injection pressure rising steadily and injectivity declining. However, field observations from several saline lacustrine carbonate reservoirs have suggested that injectivity may actually improve with continued water injection in some cases—a trend that cannot be captured by conventional simulation models. The absence of a time-dependent permeability module that accounts for dissolution-induced permeability enhancement has therefore limited the ability of reservoir engineers to forecast production performance and optimize injection strategies in these complex systems.

In this study, we conducted a systematic investigation combining high-temperature high-pressure core-flooding experiments with numerical simulation to address the following objectives; the unique contribution is an integrated workflow that measures permeability, pore-structure change and oil recovery in a single reservoir-representative core-flooding framework, and converts those measurements into a cumulative-throughput-dependent permeability model that is implemented directly into a simulator, extending previous separate experimental and reactive-transport studies such as Tan et al. and Zhang et al. [2,3]: (i) quantify the permeability response of saline lacustrine carbonate core plugs to waterflooding under reservoir-representative conditions; (ii) characterize the mineralogical and pore-structural alterations accompanying salt dissolution using NMR; (iii) establish a quantitative relationship between cumulative water throughput and permeability enhancement for implementation in reservoir simulation; (iv) develop a time-dependent permeability model and embed it as a user-defined module in a commercial simulator; and (v) evaluate the net impact of the SDPE effect on water injection performance, sweep efficiency, and ultimate oil recovery through comparative numerical simulation over a 15-year production period.

2. Materials and Methods

2.1. Core Material and Fluid Preparation

Core plugs used in this study were obtained from the Qianjiang Formation of the Jianghan Basin, a typical saline lacustrine carbonate reservoir. All plugs measured 25 mm in diameter and 50–80 mm in length, and were cleaned by Dean–Stark extraction using toluene and methanol, then dried at 60 °C to constant mass. The selected plugs covered initial porosity ranging from 5% to 18% and initial Klinkenberg-corrected gas permeability from 0.05 to 500 mD, representing a broad spectrum of reservoir types. A total of 7 plugs were tested with 3 replicates per condition; flow rates, pressure differentials, injected volumes, durations, etc. are reported in Table 1. Measurement repeatability is distinguished from independent experimental reproducibility.

Table 1. Experimental conditions and matrix.

Total Plugs/ Replicates	Flow Rate (mL/min)	Injected Volume (PV)	Duration per Test (h)	Temperature Set (°C)	Confining Pressure (MPa)	Back Pressure (MPa)	ΔP (MPa)	Repeatability
7/3 per condition	0.5	0~5	24–72	40, 80, 100	25	10, 15, 20	0.3–1.2	Independent replicate plugs agree within ±8%

X-ray diffraction (XRD) analysis showed that the bulk mineralogy consists of calcite (35–50%), dolomite (15–25%), quartz (10–15%), and feldspar (5–10%), with soluble salts (halite and anhydrite) comprising 8–15% of the rock volume (Figure 1). Backscattered

electron microscopy revealed halite occurring as intergranular cement and fracture-filling aggregates, while anhydrite appears as pore-lining cements and fine disseminations within the micritic matrix.

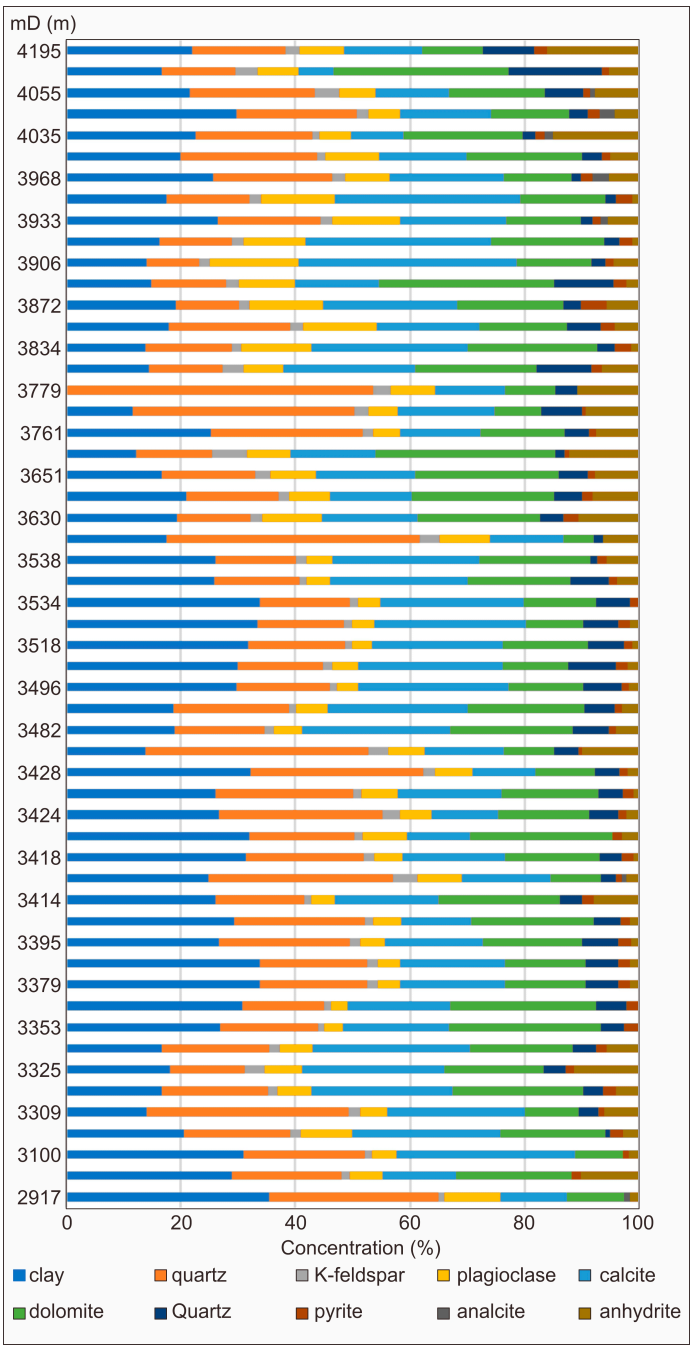


Figure 1. X-ray diffraction (XRD) patterns showing the mineral composition of representative core samples from the Qianjiang Formation.

Synthetic formation brine with a total dissolved solids (TDS) content of 180,000 mg/L was prepared to approximate the in situ water composition; full ionic compositions, preparation methods, pH, density, and viscosity for both formation and injection brines are reported in Table 2. Injection brine was prepared by diluting the formation brine to 5000–8000 mg/L TDS, representative of field injection water quality. All brines were filtered through 0.45 μm membranes and degassed under vacuum before use. The experimental matrix is shown in Table 1.

Table 2. Brine composition of the dissolution-flow experiments.

Parameter	Concentration (mg/L)							pH	Density (g/cm^3)	Viscosity (mPa·s)
	TDS	Na^+	Ca^{2+}	Mg^{2+}	Cl^-	SO_4^{2-}	HCO_3^-			
Formation brine	180,000	58,500	12,600	1800	103,500	2700	300	6.8	1.12	1.35
Injection brine	5000–8000	2100	280	65	3850	120	25	7.2	1.005	0.95

2.2. Experimental Apparatus and Core-Flooding Protocol

The displacement experiments were conducted using a customized high-pressure core-flooding apparatus consisting of three modules; Figure 2 shows a schematic of the experimental arrangement for clarity and replicability. The injection module includes an ISCO syringe pump (maximum pressure 70 MPa, flow rate 0.001–30 mL/min), intermediate vessels, and a gas pressurization system. The temperature–pressure control module comprises an air bath (room temperature to 100 °C, accuracy ±0.5 °C), a triaxial core holder (pressure rating 100 MPa), and independent confining and back-pressure control systems. The data acquisition module includes pressure transducers (accuracy 0.1% full scale), temperature sensors (±0.1 °C), a gas flow meter (0–500 mL/min, 1% full scale), an electronic balance, and a computer recording system. An NMR spectrometer (resonance frequency 2 MHz) was used for online monitoring of pore-structure changes. The NMR T_2-to-pore-size calibration is documented in Section 2.5; NMR was measured on the same core plugs before and after flooding.

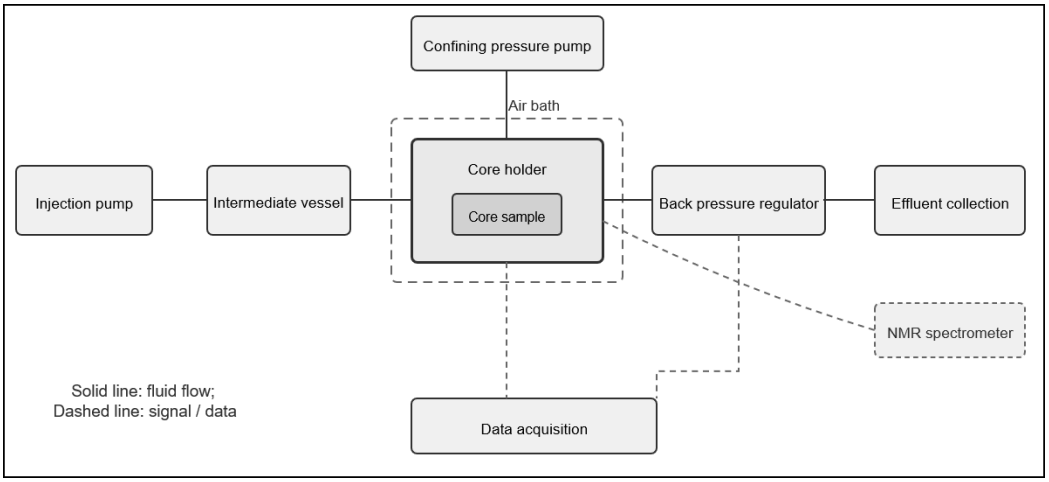


Figure 2. Schematic chart of the experimental apparatus.

Each experiment followed a systematic procedure. After vacuum-saturation with formation brine, the initial porosity, permeability, and NMR T_2 spectrum were measured under ambient conditions. Each condition was maintained for at least 2 h to reach thermal and pressure equilibrium. The core was then loaded into the holder, heated gradually to the target temperature (40, 80, 100,) at a rate of 1 °C/min; these temperatures were selected to span the shallow-to-deep reservoir temperature range of the Qianjiang Formation. The core was pressurized to a confining pressure of 25 MPa and a back pressure of 10, 15, or 20 MPa. The test fluid was then injected at a constant flow rate, with continuous recording of inlet/outlet pressures, flow rate, and temperature.

2.3. Time-Dependent Permeability Model

Based on the experimental observations, a time-dependent permeability model was developed to capture the SDPE effect at the reservoir scale. Cumulative water throughput per grid F (m^3/m^2) was introduced as the key parameter representing the dissolution history:

$$F = \int_0^t q_w(t)dt \quad (1)$$

where F is the cumulative water throughput (m^3/m^2), q_w is the water flux ($m^3/(m^2 \cdot s)$), and t is the time (s).

The permeability enhancement relationship was established by fitting the experimental data to the phenomenological correlation $K = K_0(1 + \alpha F)$, and α having reciprocal length units when F is expressed in m; the fitted data points, n, R^2, confidence intervals and residuals are shown in Table 3. The correlation is valid only within the experimental range and before complete soluble-mineral depletion. A finite mineral-inventory constraint is applied by capping the permeability update when the grid-block soluble-salt fraction reaches zero or a calibrated residual fraction.

$$K = K_0 \times (1 + \alpha \cdot F) \quad (2)$$

where K is the current permeability (mD), K_0 is the initial permeability (mD), α is the dissolution enhancement coefficient, and F is the cumulative water throughput (10^4 m^3/m^2). Based on our experimental data for the Qianjiang Formation, α ranges from 0.02 to 0.05, with higher values corresponding to higher soluble salt content or lower injection-water salinity.

Table 3. Fitting statistics for the permeability enhancement correlation.

Correlation Form	α Range	Data Points (n)	Linear Fit	Residual Range	Non-Linear Alternative	
$K = K_0(1 + \alpha F)$	0.02~0.05	36	$R^2 = 0.83$	−0.07~0.06	Power-law fit	$R^2 = 0.79$

2.4. Numerical Simulation Setup

A representative sector model was built from a typical block of the target reservoir with 120 × 80 × 45 grid cells (total 432,000 cells). Reservoir parameters were assigned based on well logs and core analysis, with porosity ranging from 0.05 to 0.18 (Figure 3), and initial permeability from 0.1 to 500 mD (Figure 4). The simulation grid, well locations and controls, PVT, relative permeability, capillary pressure, initial conditions, constraints, exact permeability-update equation and calibration procedure are documented in Table 4. The simulator version and software used to generate Figures 3 and 4 are also listed.

Two numerical simulation scenarios were designed for comparison. In Scenario I (conventional model), permeability was treated as a constant property. In Scenario II (time-dependent model), permeability was updated dynamically according to Equation (2), with α assigned in zones by interpolation of experimentally derived α values against lithofacies, soluble-salt content and injection-water salinity as documented in Table 2.

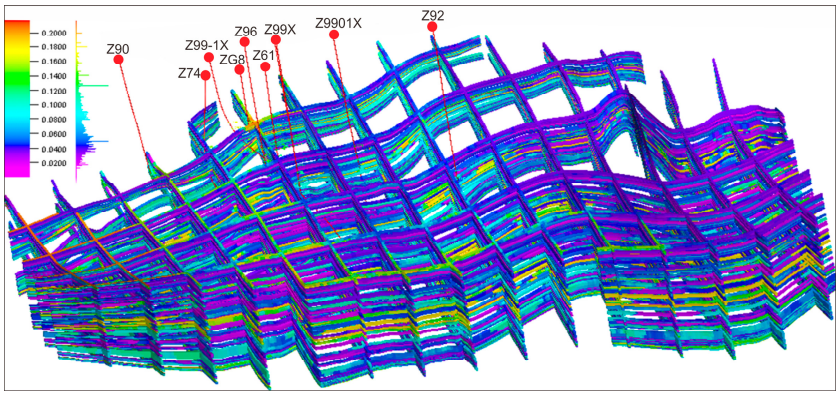


Figure 3. Porosity distribution model of the sector model extracted from the target reservoir block.

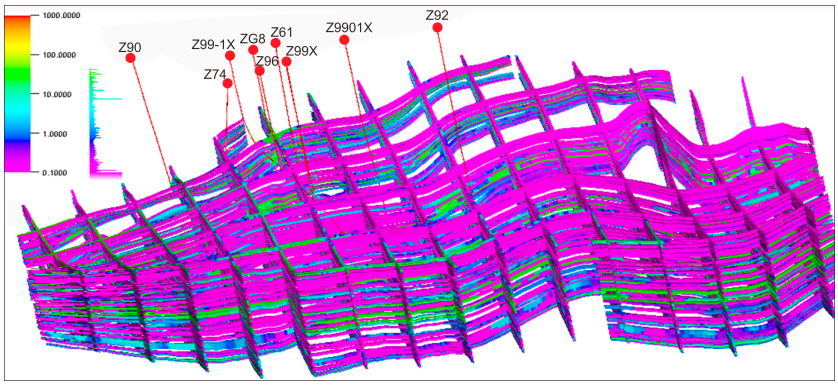


Figure 4. Initial permeability distribution model of the sector model (before accounting for the SDPE effect).

Table 4. Numerical simulation parameters.

Grid Cell Size (x, y, z)	Grid Dimensions	Porosity Range	Initial Permeability Range (mD)	Well Pattern	Model Type	Initial Pressure (MPa)	Permeability-Update Equation	α Range	Simulator
10 m × 10 m × 2 m	120 × 80 × 45	0.05~0.18	0.1~500	Inverted five-spot	Black-oil	25	$K = K_0(1 + \alpha F)$	0.02~0.05	Eclipse 2022

The simulation was run for 15 years with injection wells operating at constant injection rate and producers at constant bottom-hole pressure. Production continued until the economic limit of 98% water cut.

2.5. Data Analysis

Permeability at each condition was calculated using Darcy's law with fluid compressibility corrections; the enhancement reported in this study refers to horizontal, bedding-parallel permeability, and vertical permeability was not separately measured at plug scale. NMR T_2 spectra were inverted using a multi-exponential fitting routine with 100 logarithmically spaced bins. The uncertainty in permeability measurements was assessed through triplicate replicate analyses on adjacent plugs, giving standard deviations consistently below ±6%.

3. Results

3.1. Experimental Observations of Permeability Enhancement

The experiments revealed a consistent and significant permeability enhancement effect during waterflooding under all tested temperature–pressure conditions. The evolution of permeability exhibited three distinct phases across all samples (Figure 5, Table 5). Table 6 summarizes the main quantitative findings, including porosity, permeability, pore-throat interval, sweep efficiency and percentage mineral composition before and after waterflooding.

Table 5. Core-flooding experimental settings and results.

Core No.	K_0 (mD)	K (mD)	K/K_0	ΔK (%)	T (°C)	P (MPa)	Salt Content (%)	Uncertainty (±%)
1	3.86	9.65	2.50	150	40	10	14.2	5.5
2	6.25	13.75	2.20	120	40	15	9.8	3.1
3	0.75	2.03	2.70	170	40	15	15.1	6.8
4	0.68	1.77	2.60	160	80	20	13.7	2.9
5	2.15	5.16	2.40	140	80	20	11.2	3.8
6	5.60	14.56	2.60	160	100	20	10.5	4.2
7	28.50	42.75	1.50	50	100	20	9.1	3.5

Table 6. Summary of main quantitative findings.

Porosity Increase (%)	Pore-Throat Interval Enlarged (μm)	NMR Signal Enhancement (%)	Permeability Mode	Sweep Efficiency (%)	Recovery Factor (%)
>10	0.01~1	30~50	Constant	44	41.3
			Time-dependent	62	45.8

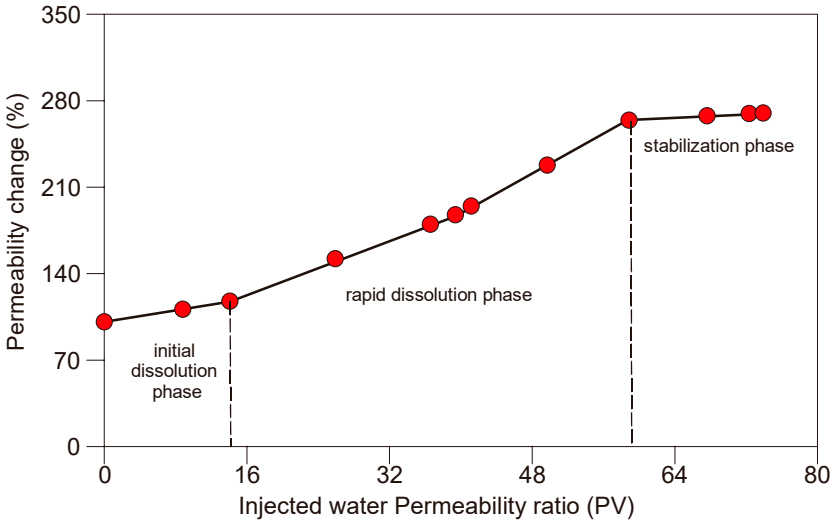


Figure 5. Permeability evolution as a function of injected pore volumes for a typical core sample, illustrating the three-stage dissolution behavior.

In the initial dissolution phase, the injected water first contacted the rock surface, and soluble salt minerals began to dissolve gradually; the dissolution front was inferred from the time evolution of pressure response, effluent ion concentrations, and post-flood imaging. Permeability increased slowly during this stage, with enhancement ranging from 10% to 30% of the initial value. The duration of this stage remained relatively short and varied inversely with temperature.

In the rapid dissolution phase, continuous water injection substantially accelerated salt dissolution, with large volumes of soluble salts being removed from the rock framework. The formation of new flow pathways resulted in a rapid increase in permeability. During this stage, the permeability enhancement reached 100–170% of the initial value. Effluent ion concentrations (Ca^{2+}, SO_4^{2-}) showed a sharp increase, confirming active mineral dissolution; cumulative effluent Na^+, Ca^{2+} and SO_4^{2-} masses were compared with the initial halite and anhydrite inventory of each core and are reported as mass-balance ratios in Table 7.

Table 7. Mass balance and mineral composition changes.

Core No.	Effluent Na^+ (g)	Effluent Ca^{2+} (g)	Effluent SO_4^{2-} (g)	Initial Halite (g)	Initial Anhydrite (g)	Na^+/Halite Ratio	SO_4^{2-}/Anhydrite Ratio
1	1.82	0.42	0.31	2.05	0.48	0.89	0.65
2	0.68	0.18	0.12	0.82	0.22	0.83	0.55
3	2.35	0.55	0.38	2.58	0.62	0.91	0.61
4	1.58	0.37	0.29	1.24	0.37	0.82	0.53
5	1.42	0.35	0.24	1.62	0.4	0.88	0.60
6	0.95	0.22	0.16	1.10	0.28	0.86	0.57
7	0.72	0.16	0.11	0.85	0.2	0.85	0.55

In the stabilization phase, after the soluble salts had been largely dissolved or after dissolution equilibrium had been reached, permeability stabilized at an elevated level without further significant change.

The magnitude of permeability enhancement depended strongly on pressure, temperature, and rock type; all enhancement quantities below are reported as percentage change $(K_1 - K_0) / K_0$ unless explicitly stated as enhancement ratio K/K_0.

Temperature exerted a controlling influence on the enhancement magnitude, with stronger ultimate enhancement observed at lower temperatures for the same pressure conditions, while initial dissolution kinetics increase with temperature. This suggests that shallower ultra-low permeability reservoirs may benefit more significantly from the SDPE effect.

3.2. Pore-Structure Evolution from NMR Analysis

NMR T_2 spectra acquired before and after the experiments provided direct evidence of pore-structure modification by salt dissolution; the T_2 relaxation time was converted to a pore-size scale using a measured surface relaxivity calibrated by mercury injection capillary pressure, so the 0.01–1 μm interval is interpreted as an equivalent pore-body radius rather than a directly measured pore-throat diameter. The most striking observation is the substantial increase in the signal amplitude in the 0.01–1 μm pore-throat interval, with the signal intensity in this range increasing by 30–50% after the flooding experiments (Figure 6). This interval corresponds to the primary flow pathways in the reservoir and is critical for fluid transport.

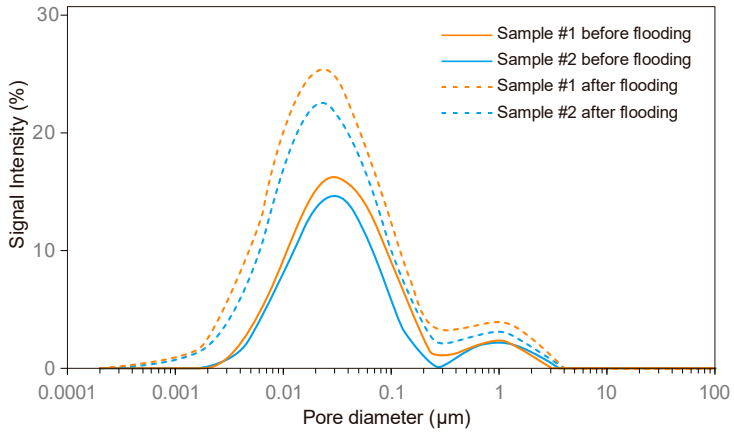


Figure 6. Comparison of NMR T_2 spectra before and after the flooding experiment, showing preferential enlargement of the 0.01–1 μm pore-throat interval.

Porosity increased by more than 10% on average after the experiments, with the magnitude of increase varying by lithology; post-flood XRD analysis showed reduced halite and anhydrite intensities while calcite remained the dominant carbonate phase, supporting dissolution of soluble salts rather than wholesale calcite removal. Grain-supported carbonate samples showed larger porosity increases (15–20%) compared with mud-dominated carbonate samples (8–12%). The pore volume increase occurred most prominently in the mesopore range, consistent with the selective dissolution of halite cement that occupied these pores.

3.3. Characteristics of High-Temperature High-Pressure Water

Under reservoir conditions (temperatures up to 100 °C, pressures up to 25 MPa), the injected water exhibits distinct physical and chemical properties that differ significantly from those at ambient conditions and that collectively contribute to the SDPE effect:

(1) Elevated temperature substantially reduces water viscosity, as expected for liquid water, and increases the diffusion coefficient. High-temperature water can penetrate more rapidly into fine pore throats, carrying dissolved salt ions away from the dissolution front. This explains why the initial dissolution rate increases with temperature, despite the smaller ultimate enhancement observed at higher temperatures.

(2) The solubility of halite and anhydrite increases substantially with temperature. Experimental data indicate that the solubility of $CaSO_4$ at 100 °C is approximately 2.5 times that at 40 °C. This enhanced solubility means that each unit volume of injected water can dissolve more salt, yielding greater permeability enhancement per unit of cumulative throughput.

(3) High-temperature high-pressure conditions reduce the oil–water interfacial tension, enabling the aqueous phase to enter smaller pores and to more effectively displace oil from the rock matrix. The altered wetting conditions allow the injected water to contact a greater fraction of the mineral surface, promoting more extensive salt dissolution.

3.4. Numerical Simulation Results

Comparison of the conventional model and the time-dependent permeability model through numerical simulation revealed substantial differences in predicted performance. In the conventional model, with constant permeability, the injection well bottom-hole pressure increased continuously with injection time, reflecting the progressive difficulty of injecting water into the reservoir. The predicted 15-year cumulative water injection was only 1.20×10^6 m^3.

In the time-dependent permeability model, the permeability of grid cells around the injection well increased progressively with cumulative water throughput. As a result, the injection pressure, after an initial rise, stabilized and then slightly declined. The predicted 15-year cumulative water injection was 1.50×10^6 m^3, an increase of 25% compared with the conventional model (Figure 7).

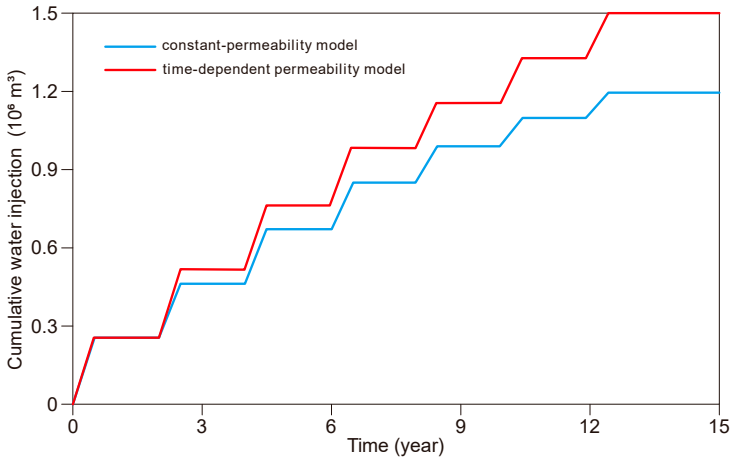


Figure 7. Comparison of cumulative water injection curves between the conventional constant-permeability model (blue) and the time-dependent permeability model (red) over 15 years of production.

Sweep efficiency analysis showed that the time-dependent permeability model achieved a sweep coefficient of 62% after 15 years, compared with 44% for the conventional model—an improvement of 18 percentage points. The dynamic evolution of high-permeability pathways guided the injected water to regions that would not have been effectively swept in the conventional model (Figure 8).

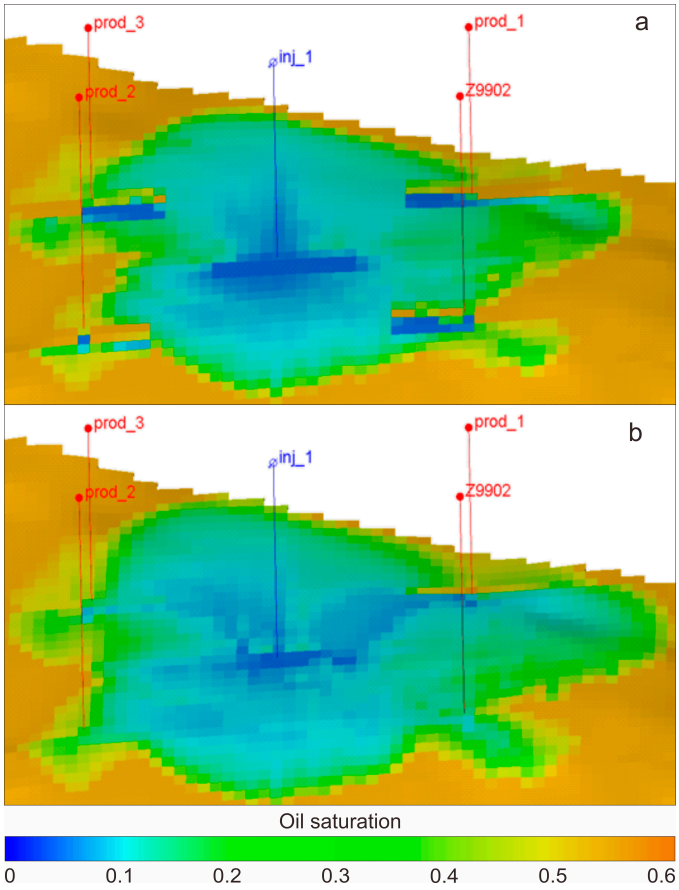


Figure 8. Comparison of oil saturation distributions at the end of 15-year production between (**a**) the conventional constant-permeability model and (**b**) the time-dependent permeability model.

The improvement in ultimate oil recovery was equally significant. The conventional model predicted a recovery factor of 41.3% after 15 years, while the time-dependent model predicted a recovery factor of 45.8%—an improvement of 4.5 percentage points absolute (Figure 9). A sensitivity analysis across heterogeneous soluble-salt distributions and permeability fields shows that the recovery benefit varies with spatial distribution, indicating that the sign of the effect is robust but its magnitude is case-dependent. The grid-scale statistics reveal that recovery improvement was most pronounced in low-permeability intervals, where the additional recovery reached 6.2 percentage points, compared with 2.5 percentage points in high-permeability intervals.

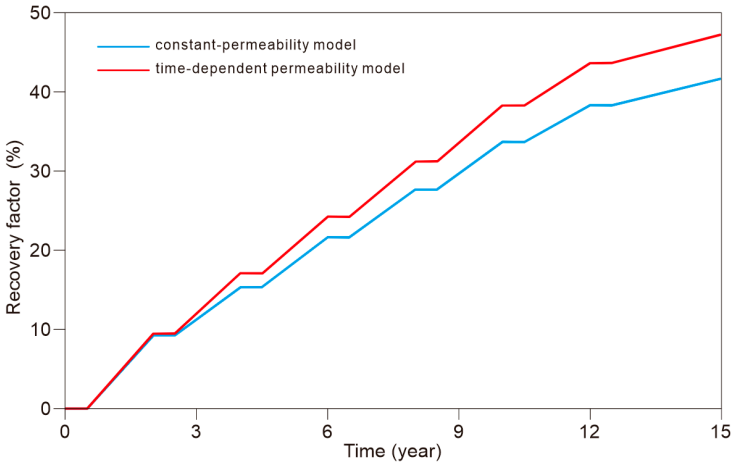


Figure 9. Comparison of recovery factor curves between the conventional constant-permeability model (blue) and the time-dependent permeability model (red) over 15 years of production.

4. Discussion

4.1. Mechanistic Interpretation of the SDPE Effect

The experimental results establish a clear mechanistic sequence linking injection-water undersaturation, evaporitic mineral dissolution, pore-throat enlargement, and macroscopic permeability increase. The permeability response follows a three-stage pattern: initial slow dissolution, rapid permeability improvement, and final stabilization. The maximum enhancement of 170% observed in this study is comparable to, though somewhat higher than, reported values from similar carbonate–evaporite systems; the specific enhancement values and conditions from [1,16] are tabulated for direct comparison in Table 5. This difference likely reflects the higher soluble salt content (8–15%) of the Qianjiang Formation samples relative to those examined in earlier studies.

NMR analysis provides direct evidence that dissolution preferentially targets the 0.01–1 μm pore-throat interval, with signal intensity in this range increasing by 30–50%. Because permeability scales approximately as the square of the critical throat radius [19], a comparatively small volumetric dissolution of halite—on the order of a few pore volume percent—is capable of producing the substantial permeability enhancement observed here; the NMR signal enhancement was quantified as the change in integrated T_2-bin amplitude over the 0.01–1 μm range.

This mechanism is inferred to operate in parallel with chemical dissolution; a combined effect is plausible, but the relative causal contributions of dissolution and pressure effects were not quantitatively separated in this study.

4.2. Implications for Waterflooding Design

The time-dependent permeability model developed in this study provides a practical tool for incorporating the SDPE effect into reservoir simulation. The comparison between the conventional and time-dependent models reveals that accounting for permeability evolution significantly alters the predicted performance: cumulative water injection increases by 25%, sweep volume expands by 18%, and ultimate recovery improves by 4.5 percentage points.

Several practical implications follow from these results. First, the enhancement is most valuable in the early stages of waterflooding, when the dissolution front is actively expanding, and the permeability improvement directly facilitates better injectivity. Second, the recovery benefit is more pronounced in low-permeability intervals (6.2 percentage points) than in high-permeability intervals (2.5 percentage points), suggesting that the SDPE effect may be particularly beneficial for tight reservoir zones that would otherwise be difficult to develop. Third, the magnitude of enhancement is sensitive to the dissolution coefficient α, which depends on injection-water salinity and soluble salt content.

The distinct pressure responses between the two models also offer a potential diagnostic tool. The pressure decline observed in the time-dependent model, as opposed to the monotonic rise in the conventional model, could be monitored in field waterfloods through downhole pressure gauges. A flattening or declining injection pressure trend may indicate active salt dissolution and permeability enhancement, whereas a rising trend may suggest the absence of such effects or the presence of formation damage; these trends are non-unique and should be interpreted together with reservoir heterogeneity, wellbore effects, and other operational changes.

4.3. Limitations

Several limitations of this study should be acknowledged. The experiments were conducted on small-diameter plugs, and meter-scale heterogeneity may alter dissolution patterns in ways that cannot be captured at the plug scale. Upscaling the SDPE model from

the laboratory to the field scale requires further work, particularly regarding the spatial distribution of soluble minerals. In addition, only one reservoir system (the Qianjiang Formation) was examined, and generalization to other saline lacustrine carbonate reservoirs requires additional validation. The experimental timescales are also far shorter than reservoir flooding timescales, and the long-term behavior of the SDPE effect under continuous water injection remains uncertain. Geomechanical effects were not explicitly considered in the current model. Additional limitations include the small plug-to-field scale, the narrow range of oil viscosity tested, constant flow-rate conditions, and the absence of geochemical modeling to track downstream reprecipitation of dissolved ions.

5. Conclusions

(1) High-temperature high-pressure core-flooding experiments confirmed a significant salt dissolution–induced permeability enhancement effect. Under reservoir-representative conditions, permeability increased by up to 170%.

(2) NMR analysis revealed that salt dissolution preferentially enlarged the 0.01–1 μm pore-throat interval, with 30–50% signal enhancement in this range.

(3) A time-dependent permeability model was established using cumulative water throughput per grid as the key parameter: $K = K_0 \times (1 + \alpha \cdot F)$. The model was implemented as a user-defined module in a commercial simulator, enabling dynamic permeability updates based on local injection history.

(4) The recovery benefit is more pronounced in low-permeability intervals (6.2 percentage points) than in high-permeability intervals (2.5 percentage points). Comparative numerical simulation between the conventional constant-permeability model and the time-dependent model showed that accounting for the SDPE effect increases predicted cumulative water injection by 25%, expands sweep volume by 18 percentage points absolute, and improves ultimate oil recovery by 4.5 percentage points absolute over 15 years of production; these results assume a time-invariant α and Darcy-scale permeability updates, and may overestimate recovery where wormhole formation dominates.

(5) The methodology developed in this study—combining experimental quantification, derivation of a time-dependent permeability model, and implementation in reservoir simulation—provides a quantitative framework for optimizing waterflooding design in salt-bearing carbonate reservoirs with measurable soluble-salt content, such as the 8–15% range investigated here, and for predicting when salt dissolution will enhance rather than impair recovery. Future work should extend validation to other reservoirs, calibrate α over a wider salinity and salt-content range.

Author Contributions: Conceptualization, H.W. and C.C.; methodology, H.W.; software, C.C.; validation, B.Y. and L.Z.; formal analysis, L.H. and M.Z.; investigation, B.W. and X.W.; resources, X.W.; data curation, H.W. and C.C.; writing—original draft preparation, H.W.; writing—review and editing, C.C., B.Y., L.Z., L.H., M.Z., B.W. and X.W.; visualization, M.Z.; supervision, C.C.; project administration, C.C.; funding acquisition, C.C. All authors have read and agreed to the published version of the manuscript.

Funding: This research was funded by SINOPEC, grant number P24053.

Data Availability Statement: The original contributions presented in this study are included in the article. Further inquiries can be directed to the corresponding author.

Acknowledgments: During the preparation of this manuscript/study, the authors used DeepSeek V4.0 for the purposes of language checking. The authors have reviewed and edited the output and take full responsibility for the content of this publication.

Conflicts of Interest: Authors Hua Wu, Chenguang Cao, Bo Yin, Liang Zhang, Lishi Huang, Manting Zhang and Boyu Wang were employed by the Institute of Exploration and Development of SINOPEC Jianghan Oilfield Company. The remaining authors declare that the research was conducted in the absence of any commercial or financial relationships that could be construed as a potential conflict of interest. The authors declare that this study received funding from SINOPEC. The funder was not involved in the study design, collection, analysis, interpretation of data, the writing of this article or the decision to submit it for publication.

Abbreviations

The following abbreviations are used in this manuscript:

SDPE	salt dissolution–induced permeability enhancement
XRD	X-ray diffraction
NMR	nuclear magnetic resonance
PV	pore volume
TDS	total dissolved solids

References

1. Tan, Q.; You, L.; Kang, Y.; Zhang, X.; Meng, S. Changes in pore structures and porosity-permeability evolution of saline-lacustrine carbonate reservoir triggered by fresh water-rock reaction. *J. Hydrol.* **2020**, *580*, 124375. [CrossRef]
2. Tan, Q.; Kang, Y.; You, L.; Peng, H.; Zhao, F.; Bai, J. The role of salt dissolution on the evolution of petrophysical properties in saline-lacustrine carbonate reservoirs: Pore structure, porosity–permeability, and mechanics. *J. Hydrol.* **2023**, *618*, 129257. [CrossRef]
3. Zhang, R.; Wang, T.; Wang, F.; Zhu, X.; Wang, Y.; Kou, S.; Wang, J. Time variation flow model of reservoir permeability based on effective cumulative water flux. *Pet. Geol. Recovery Effic.* **2025**, *32*, 162–173.
4. Zhang, Q.; Zhang, L.; Liu, Q.; Jiang, Y. Pressure performance of highly deviated well in low permeability carbonate gas reservoir using a composite model. *Energies* **2020**, *13*, 5952. [CrossRef]
5. Cai, N.; Wang, W.; Xiao, G.; Yang, Z.; Zhu, H.; Wang, X. Geochemical Characteristics and Origin of Heavy Metals and Dispersed Elements in Qarhan Salt Lake Brine. *Water* **2025**, *17*, 1927. [CrossRef]
6. Ganguli, S.S.; Dimri, V.P. Reservoir characterization: State-of-the-art, key challenges and ways forward. In *Developments in Structural Geology and Tectonics*; Elsevier: Amsterdam, The Netherlands, 2023; Volume 6, pp. 1–35.
7. Sun, Z.; Li, Z.; He, C.; Zhu, F.; Shen, B.; Lu, L. Characteristics of connected pores and evaluation of shale oil mobility in the Qianjiang Formation, Qianjiang Sag, Jianghan Basin, China. *J. Earth Sci.* **2025**, *36*, 1591–1604. [CrossRef]
8. Cao, C.; Liu, X.; Wu, H.; Zhang, L.; Jia, Y.; Zhang, M.; Wang, X. Characteristics of fractured lacustrine carbonate reservoirs in the Zhongshi area, Jianghan Basin, China. *Energies* **2026**, *19*, 1402. [CrossRef]
9. Liang, X.; Chen, F.; Li, W.; Wu, Z.; Ma, W. The controlling effect of salt rhythm in continental saline lake basins on tight oil accumulation: A case study of the lower Xinguozui Formation in the Qianjiang Sag. *Resour. Data J.* **2026**, *5*, 116–123.
10. Yang, Y.; Yang, Y. Effect of water injection rate on the distribution of water-driven oil in the Tankou Oilfield. *J. GeoEnergy Environ.* **2026**, *2*, 163–177. [CrossRef]
11. Alvarado, V.; Manrique, E. Enhanced oil recovery: An update review. *Energies* **2010**, *3*, 1529–1575. [CrossRef]
12. Buckley, S.E.; Leverett, M.C. Mechanism of fluid displacement in sands. *Trans. AIME* **1942**, *146*, 107–116. [CrossRef]
13. Abbasi, S.; Khamehchi, E. Investigation of permeability decline due to coupled precipitation/dissolution mechanism in carbonate rocks during low salinity co-water injection. *Energy Rep.* **2021**, *7*, 125–135. [CrossRef]
14. Xun, Y.; Xiao, J.; Shi, L. A novel numerical simulation method for oil reservoir considering time-varying permeability. *Geosyst. Eng.* **2025**, *28*, 524–530. [CrossRef]
15. Ellis, B.R.; Fitts, J.P.; Bromhal, G.S.; McIntyre, D.L.; Tappero, R.; Peters, C.A. Dissolution-driven permeability reduction of a fractured carbonate caprock. *Environ. Eng. Sci.* **2013**, *30*, 187–193. [CrossRef] [PubMed]
16. Niu, B.; Krevor, S. The Impact of Mineral Dissolution on Drainage Relative Permeability and Residual Trapping in Two Carbonate Rocks. *Transp. Porous Media* **2020**, *131*, 363–380. [CrossRef]
17. Stiller, M.; Yechieli, Y.; Gavrieli, I. Rates of halite dissolution in natural brines: Dead Sea solutions as a case study. *Chem. Geol.* **2016**, *447*, 161–172. [CrossRef]
18. Colombani, J.; Bert, J. Holographic interferometry study of the dissolution and diffusion of gypsum in water. *Geochim. Cosmochim. Acta* **2007**, *71*, 1913–1920. [CrossRef]
19. Blunt, M.J.; Bijeljic, B.; Dong, H.; Pentland, C. Pore-scale imaging and modelling. *Adv. Water Resour.* **2013**, *51*, 197–216. [CrossRef]

20. Menke, H.P.; Andrew, M.G.; Vila-Comamala, J.; Rau, C.; Blunt, M.J.; Bijeljic, B. Dynamic pore-scale reservoir-condition imaging of reaction in carbonates using synchrotron fast tomography. *J. Vis. Exp.* **2017**, *120*, e53763. [CrossRef] [PubMed]
21. Sharma, H.; Kishore, K.M. Modeling of low salinity waterflooding in carbonates: Effect of rock wettability and organic acid distribution. *J. Pet. Sci. Eng.* **2022**, *208*, 109624. [CrossRef]
22. Bartels, J.; Kühn, M.; Clauser, C. *Numerical Simulation of Reactive Flow Using SHEMAT*; Springer: Berlin/Heidelberg, Germany, 2003; pp. 5–74.
23. Elkhoury, J.E.; Ameli, P.; Detwiler, R.L. Dissolution and deformation in fractured carbonates caused by flow of CO_2-rich brine under reservoir conditions. *Int. J. Greenh. Gas Control* **2013**, *16*, S203–S215. [CrossRef]
24. Tan, Q.; Yang, B.; You, L.; Kang, Y.; Peng, H.; Song, F.; Lin, C. Drill-in fluid optimization for formation damage control considering salt dissolution in saline-lacustrine reservoirs. *SPE J.* **2004**, *29*, 1271–1288.
25. Golfier, F.; Zarcone, C.; Bazin, B.; Lenormand, R.; Lasseux, D.; Quintard, M. On the ability of a Darcy-scale model to capture wormhole formation during the dissolution of a porous medium. *J. Fluid Mech.* **2002**, *457*, 213–254. [CrossRef]
26. Chen, X.; Huang, Q.; Liu, P.; Du, J.; Guo, Y.; Xiong, Z. Numerical simulation of CO_2 sequestration stability in carbonate-bearing saline aquifers: Effects of mineral dissolution. *Energy* **2025**, *375*, 138273. [CrossRef]

Disclaimer/Publisher's Note: The statements, opinions and data contained in all publications are solely those of the individual author(s) and contributor(s) and not of MDPI and/or the editor(s). MDPI and/or the editor(s) disclaim responsibility for any injury to people or property resulting from any ideas, methods, instructions or products referred to in the content.